CHANGES IN THE REFLECTED SPECTRA OF EMBEDDED CHIRPED FIBRE BRAGG GRATINGS USED TO MONITOR DISBONDING IN BONDED COMPOSITE JOINTS

J Palaniappan[1], H Wang[1], S L Ogin[1,*], A M Thorne[1], G T Reed[2], A D Crocombe[1] and S C Tjin[3]

[1]School of Engineering, University of Surrey, GU2 7XH, UK

[2]Advanced Technology Institute, School of Electronics and Physical Sciences, University of Surrey, GU2 7XH, UK

[3]School of Electrical and Electronic Engineering, Photonics Research Centre, Nanyang Technological University, Singapore

*E-mail: S. Ogin@surrey. ac. uk (tel : 0044 1483 689614 ; fax : 0044 1483 686291)

ABSTRACT

Recent work has outlined a method for health monitoring the structural integrity of adhesively bonded composite joints based on the use of a chirped fibre Bragg grating (CFBG) embedded within an adherend, but not within the glue-line. In this paper, the reflected CFBG spectra for disbonds of different lengths have been predicted with the aid of a finite-element model of the strain field resulting from a disbond and commercially available software for predicting the reflected spectra of fibre Bragg grating sensors. The modelling shows the relationship between the position of the disbond front and the dip in the reflected spectrum which moves to higher wavelengths as the disbond extends. These results enable visual observations of the disbond front in the optically transparent joint to be compared with the CFBG results, showing that the sensor can determine the disbond front position to within a few millimetres. For other bonded structures, this resolution is likely to be determined largely by the adherend materials and sensor position.

Keywords: A. Adhesive joints; B. Disbonding; C. Finite element analysis (FEA); D. Non-destructive testing

INTRODUCTION

Adhesive bonding of composite structures is an attractive alternative to mechanical fasteners because stresses are distributed over the entire bond area. However, as is well known, a major concern for bonded joints is the initiation and growth of a failure in the form of a disbond between adherends in either quasi-static or fatigue loading. A number of NDE (non-destructive evaluation) methods have been suggested to monitor bonded joints based on ultrasonic [1,2], acoustic [3], radiographic, thermal [4] and backface strain measurements [5]. Notwithstanding the advantages of each technique, it would be useful to have a method that can both indicate

when disbond initiation has occurred and can monitor the subsequent change in the position of the disbond to within a few millimetres.

The use of optical fibre sensors, particularly fibre Bragg gratings, for health monitoring composite and other structures is progressing rapidly [6-8]. Of the various optical fibre sensors available, uniform fibre Bragg grating (FBG) sensors are being employed for various applications. These sensors have a uniform periodic perturbation in the refractive index of the fibre core. When broadband light is coupled into the optical fibre sensor, a reflection peak is obtained, centred on a wavelength called the Bragg wavelength, which depends on the refractive index and the period of the grating. These sensors can be used to monitor both strain and damage development [9-12]. Such sensors are also finding applications for internal strain monitoring in composite ship structures and patch repairs [13-16].

This paper focuses on modelling the results of a novel technique for monitoring disbond development using a special type of FBG called a chirped fibre Bragg grating (CFBG). The CFBGs used in this work have a linear variation of the grating period and reflect a spectral band of wavelengths corresponding to the grating spacings within the sensor. Okabe, Takeda and colleagues have shown, in a series of papers [17,18], that such a sensor can be used to monitor matrix crack development and crack position in cross-ply CFRP laminates, and Palaniappan et al [19] have demonstrated how the precise crack position is related to the reflected spectrum with the aid of transparent GFRP laminates. Takeda and colleagues [20] have also demonstrated the possibility of monitoring delamination initiation and growth in a composite laminate using a CFBG.

In recent work [21], we have shown that changes in the reflected spectrum from a CFBG embedded within one of the adherends of a bonded joint are related to the growth due to fatigue cycling of a disbond between the adherends. In the current paper, these experimental results are reviewed briefly, and a finite-element model of the joint is presented which, in conjunction with commercially available software for predicting FBG spectra, enables characteristic features of the reflected spectrum to be related to the actual position of the disbond front in the joint.

BACKGROUND

Bonded joints fabricated using two adherends of a transparent GFRP were used for these experiments [21]. The overlap length of the lap joint is also transparent, enabling the propagation of the disbond to be monitored visually during the tests, for direct comparison with the measurements made using the CFBG. Double cross-ply, frame-wound GFRP laminates were used for the adherends, with the laminate configuration being $(0_2/90/0_6)_s$ and an individual ply thickness of 0.25 mm (giving a total laminate thickness of 4.5 mm). CFBGs, 45 mm in length with a full width at the half maximum of the reflected spectrum of 20 nm, were embedded within the 0^0 plies of the double crossply laminate during fabrication near the first 0/90 interface, and hence approximately 0.5 mm from the laminate surface. The adherends required to manufacture the bonded joint were 20 mm wide and 120 mm long with an overlap length of 60 mm.

The adherends containing the embedded sensors were cut so that the low wavelength end of the CFBGs was adjacent to the cut end of the adherend. For this to be possible, it was necessary to discriminate between the low and high wavelength end of the sensor by applying a simple through-thickness load using a small finger-tightened clamp mounted onto the coupon; this loading produces a perturbation in the reflected spectrum which enables the low-wavelength end of the sensor to be identified, as shown in Figure 1 (interestingly, recent work by Swart et al [22] has demonstrated the potential of a CFBG as a pressure sensor). The coupon was then cut so that the low wavelength end of the chirped grating lay at the cut end of the adherend. The adhesive used to manufacture the bonded joint was an elevated temperature cure adhesive (AV 119) and the joint was cured at 120º C for 1 hour; a schematic diagram of the joint is shown in Figure 2. A uniform thickness of adhesive between the adherends was achieved by using aluminium wires with a diameter of 0.40 mm as spacers and the bond was formed under light pressure in a finger-tightened jig. The bonded joints were subjected to fatigue with a peak load of 11 kN, (corresponding to an adherend tensile stress of 122 MPa) and an R-value ($R= \sigma_{min}/\sigma_{max}$) of 0.1, using a sinusoidal waveform with a frequency of 3 Hz. The optical arrangement consisted of a broadband light source, coupler and optical spectrum analyser (details are provided in [19, 21, and 23]). Optical reflection spectra were recorded after interrupting the test at increasing numbers of cycles and with the joint

subjected to a small load of 5 kN. Images of the progression of the disbonds in the transparent joints were also captured *in situ* using a digital camera.

Detection of disbond initiation is illustrated in Figure 3. Figure 3(a) shows an image of the bonded region of the joint after 8000 fatigue cycles and Figure 3(b) shows a comparison of the reflected spectra after 2000 and 8000 cycles. After 2000 cycles, no disbonding had occurred in the joint, whereas a disbond has just begun to form at the joint overlap marked A in Figure 3(a) at around 8000 cycles. The reflected spectra shown in Figure 3(b) show distinct differences at low-wavelengths because the consequence of the onset of disbonding is to unload the adherend, and hence the CFBG sensor is also unloaded local to the disbond. This relaxes the grating spacing so that reflections at lower wavelengths are seen. No changes occurred to the spectrum at higher wavelengths so that, for example, the dip in the spectrum due to the position of the wire spacer remains unchanged (the adhesive bond was formed under light pressure and the local strains in the composite due to the presence of the wire spacer locally modified the reflected spectrum, indicating the wire position).

Detection of disbond propagation is shown in Figures 4 and 5. In Figure 4, the development of disbonds at each end of the joint is evident and the position of the disbond monitored by the CFBG after 9000, 10,500 and 13,400 cycles is indicated by the arrows B, C and D. The reflected spectra recorded at each of these cycles are shown in Figure 5. The position of the disbond was associated with a dip in the reflected spectrum and as the disbond grew in length, the dip in the spectrum moved to higher wavelength values. This dip in the reflected spectrum is due to the load redistribution at the disbond front. The modelling work, discussed in the next section, establishes the relationship between the dip in the spectrum and the actual position of the disbond front.

MODELLING THE REFLECTED SPECTRA

Finite element modelling

2D FE modelling was undertaken to predict the axial strain experienced by the optical fibre as a consequence of the disbond. At this stage, the optical fibre has not been included explicitly in the model, but the strains have been extracted from the FE model at the location of the fibre. Since the fibre is positioned in the centre of the

adherend (in a widthwise sense), plane strain finite elements were used. Three linear material models were created and assigned to the adhesive, the 0^o ply and the 90^o ply respectively. The properties are summarised in Tables 1 and 2 for the isotropic (adhesive) and orthotropic (composite) materials respectively.

Initially a joint with no disbond was modelled and a number of mesh schemes were assessed with decreasing mesh size, down to the finest mesh considered, which had an element size of 0.05 mm x 0.05 mm. It was found that the results had converged for the mesh where the smallest element was 0.1 mm x 0.1 mm and hence this mesh was used in the remainder of the study. Geometric non-linearity was investigated also, but this was found to have an insignificant effect on the results and hence was not used in the rest of the work.

Figure 6 shows the strain distribution around the low strain region of the optical fibre. The white bands were obtained by not displaying the 90^o plies. Hence, moving from the first 0/90 interface in the upper adherend, there is 0.5 mm of the 0^0 ply (upper adherend), then the more compliant adhesive, then the 0^0 ply of the second adherend, before reaching the first 0/90 interface in the second adherend. It can be seen that at the free end of the adherend, the longitudinal direct strains (E11) are low (as expected). As the load transfers from the lower, loaded adherend through the adhesive to the upper adherend, the strains in the upper adherend begin to increase with increasing distance from the end of the adherend.

The longitudinal strains (E11) along the centreline at the position of the optical fibre were extracted from the results and are plotted in Figure 7 for three cases: no disbond, disbond 5 mm in length and disbond 10 mm in length; a higher magnification view of the first 20 mm of the overlap region for each case is shown in Figure 8. For the "no disbond" case, the data show the trend described above, i.e. starting from a low stress value near the end of the adherend and increasing to a plateau region after about 5 mm. The plateau region is, of course, the result of no load transfer at the centre of what is a long joint. The strains then increase again as the other end of the overlap is approached and the load transfer process begins again with loads transferred from the second adherend.

For the two other cases, i.e. 5 mm disbond and 10 mm disbond, the models were run with the disbonds positioned on the lower adhesive-adherend interface, which is consistent with the observed experimental

disbond path. Figure 9 shows the strain distribution for the case of a 10 mm disbond. This time the maximum strain shown has been limited and the region coloured grey indicates strains above this set value. The strain distribution is made more complex by the presence of the crack. It can be seen that the right hand, "free" part of the upper adherend experiences low values of strain as expected. These increase as the load is transferred from the lower adherend, through the adhesive to the upper adherend. Again, the path of the optical fibre runs just below the marked 0/90 interface. The longitudinal strain distributions for the 5 mm and 10 mm cracked models are also shown in Figures 7 and 8. It can be seen that these strain distributions differ only in the region where the disbond exists. Essentially, the disbond increases the unstrained length of the adherend. Interestingly, the small perturbation in the strain distribution at the beginning for each case is not an artefact of the mesh size. Meshes with element sizes significantly smaller than the distance of these perturbations from the overlap end (0.1 mm and 0.05 mm) showed that these perturbations are a characteristic feature of the strain field within the adherend a small distance from the bondline. The perturbation in the cracked cases is made more complicated by the interaction of the disbond front strain field and the load transfer strain field. For example, tracking right to left, below but close to the 0/90 interface in the contour plot of Figure 9, it will be seen that the strain rises and falls in advance of the position of the disbond front, before rising to the plateau value.

Prediction of the reflected spectra

The finite element modelling provides the strain field required to predict the reflected spectra. OptiGrating software [24] requires the strain to be input as a function of distance, and to achieve this, the rather complicated longitudinal strain distributions have been input as three functions (there is an alternative approach to such modelling, by modifying the refractive index and grating spacing, which Okabe, Takeda and colleagues have used; e.g.[18,20]). A comparison of the input longitudinal strain distribution (Figure 10) and the actual strain distribution obtained from the FE analysis show that these are almost identical in advance of the plateau, and differ by no more than 6% in the plateau region where small strain changes are unimportant with regard to the reflected spectrum. The other parameters used in the OptiGrating prediction are: uniform apodization, Poisson's ratio of 0.17 and photoelastic coefficients p_{11}=0.121 and p_{12}=0.27, with an index modulation, Δn, of 0.0003.

Figure 11 shows the predicted reflected spectra for disbonds of length 5 mm and 10 mm, together with the actual position of the disbond front used in the modelling. The simulations show that the small perturbation in the strain field in advance of the disbond front produces a small dip in the reflected spectrum which, however, is not seen in the experimental results, possibly because this small dip has a similar magnitude to the noise in the spectrum. The important feature of the predicted spectra is the large dip, and it is clear from the simulations that the minimum of the large dip is not the actual position of the disbond front. The disbond front is located about 1.5 mm away from the minimum in the reflected spectrum, shown by the vertical line in Figures 11(a) and 11(b), towards the low wavelength end of the CFBG. Figure 12 shows a superposition of the predicted reflection spectra for the disbond lengths of 5 mm and 10 mm; the form of the spectra is in good agreement with the experimental results of Figure 7.

Clearly, the key feature of the strain distribution in the region of the disbond is the sharp rise in strain just ahead of the disbond front, which is the stress transfer region. This rapidly changing strain causes the loss of particular pitch lengths in the fibre Bragg grating, producing a fall in intensity of the reflected spectrum at particular wavelengths and a corresponding increase in intensity at other wavelengths, which is the origin of the pronounced dip in the spectrum and a direct indication of the current position of the disbond front. Figure 13 shows the position of the disbond front obtained from the CFBG spectra (corrected for the actual position of the disbond front in relation to the minimum of the dip in the spectrum) compared with the measured position of the disbond front obtained from images of the bonded joint. Overall, the CFBG technique enables the disbond front to be located to within about 2 mm for this bonded joint. It is anticipated that, in general, the accuracy of the CFBG technique in locating the disbond front will depend primarily on the materials used to form the bond and the distance of the CFBG sensor from the bond line.

CONCLUSIONS

Disbond *initiation* and disbond *growth* have been monitored in a bonded joint by embedding chirped fibre Bragg grating sensors within GFRP composite adherends (i.e. the sensors are *not* located within the bondline). The sensors were embedded with the low-wavelength end of the CFBG adjacent to the end of one adherend.

Disbond initiation is detected as a shift of the low-wavelength end of the reflected spectrum to lower wavelengths (as a consequence of the unloading of the adherend due to disbond formation), while the remainder of the spectrum is unchanged. Disbond *growth* can be monitored by the movement of a dip in the reflected spectra to higher wavelengths as the disbond length increases; this dip is related to changes in the grating spacings in the stress-transfer region of the joint. The reflected spectra have been predicted using a combination of finite-element analysis (to obtain the strain distribution) and commercially available software (to predict the reflected spectrum based on the strain distribution). The modelling shows that the physical position of the disbond front in this joint does not correspond to the minimum of the dip in the reflected spectrum, but lies about 1.5 mm away from the minimum, towards the low-wavelength end of the sensor. Comparison of the CFBG results with photographs of the position of the disbond front shows that the technique has enabled the disbond front to be located to within 2 mm using the CFBG sensors.

ACKNOWLEDGEMENTS

JP would like to thank the University of Surrey for the provision of a University Research Scholarship. The authors would like to acknowledge the help of Dr Brian Le Page and Mr Peter Haynes in fabricating the laminates.

REFERENCES:

1. Cawley P. Ultrasonic measurements for the quantitative NDE of adhesive joints - potential and challenges. Ultrasonics symposium. Proc. IEEE 1992; p.767-772.
2. Hanneman SE, KinraVK, Zhu C. A low-frequency ultrasonic-spectroscopy technique for NDE of adhesive joints. Proc. 18th Annual Review, Review of progress in quantitative nondestructive evaluation 1991;11B:1267-1274.
3. Lowe MJS , Challis RE, Chan CW. The transmission of Lamb waves across adhesively bonded lap joints. J. Acous. Soc. Am. 2000;107/3:1333-1345.

4. Meola C, Bruzzone A, Giorleo L, Morace RE, Vitiello A. Application of lock-in thermography in nondestructive evaluation of adhesively-bonded aluminum joints. J. Adhesion Sci. and Tech. 2004;18/6:635-654.
5. Crocombe AD, Ong CY, Chan CM, Wahab MA, Ashcroft IA. Investigating fatigue damage evolution in adhesively bonded structures using backface strain measurement. J. Adhesion 2002;78/9: 745-778.
6. Kuang KSC, Cantwell WJ. Use of conventional optical fibers and fiber Bragg gratings for damage detection in advanced composite structures: A review. Appl. Mech. Rev. 2003;56:493-513.
7. Merzbachery CI, Kersey AD, Friebele EJ. Fiber optic sensors in concrete structures: A Review. Smart Mater. Struct. 1996;5/2:196–208.
8. Culshaw B, Michie C, Gardiner P, McGown A. Smart structures and applications in civil engineering. Proc. IEEE 1996;84/1:78-86.
9. Botsis J, Humbert L, Colpo F, Giaccari P. Embedded fiber Bragg gratings sensor for internal strain measurements in polymeric materials. Opt. Lasers Eng. 2005;43:491-510.
10. Kang H , Park J , Kang D , Kim C , Hong C, Kim C. Strain monitoring of a filament wound composite tank using fiber Bragg grating sensors. Smart Mater. Struct. 2002;11:848-853.
11. Ling HY, Lau KT, Li C. Determination of dynamic stress profile and delamination detection of composite structures using embedded multiplexed fibre-optic sensors. Compos. Struct. 2004; 66:317–326.
12. Takeda S, Minakuchi S, Okabe Y, Takeda N. Delamination monitoring of laminated composites subjected to low-velocity impact using small-diameter FBG sensors. Compos. Part A 2005;36:903-908.
13. McKenzie I, Jones R, Marshall IH, Galea S. Optical fibre sensors for health monitoring of bonded repair systems. Compos. Struct. 2000;50/4 :405-416.
14. Herszberg I, Li HCH, Dharmawan F, Mouritz AP, Nguyen M, Bayandor J. Damage assessment and monitoring of composite ship joints. Compos. Struct. 2005;67:205–216
15. Jones R, Galea S. Health monitoring of composite repairs and joints using optical fibres. Compos. Struct. 2002;58/3:397-403.

16. Li HCH, Herzsberg I, Mouritz AP, Davis CE, Galea SC. Sensitivity of embedded fibre optic Bragg grating sensors to disbonds in bonded composite ship joints. Compos. Struct. 2004; 66:239- 248.
17. Takeda N, Okabe Y, Tsuji R, Takeda S. Application of chirped fiber Bragg grating sensors for damage identification in composites. Proc. SPIE 2002;4694:106-117.
18. Okabe Y, Tsuji R, Takeda N. Application of chirped fiber Bragg grating sensors for identification of crack locations in composites. Compos. Part A 2004;35 /1:59-65.
19. Palaniappan J, Wang H, Ogin SL, Thorne AM, Reed GT, Tjin SC, McCartney LN. Prediction of the reflected spectra from chirped fibre Bragg gratings embedded within cracked crossply laminates. Meas. Sci. Technol. 2006;17/6:1609-1614.
20. Takeda S, Okabe Y, Takeda N. Application of chirped FBG sensors for detection of local delamination in composite laminates. Proc. SPIE 2003;5050:171-178 .
21. Palaniappan J, Wang H, Ogin SL, Thorne AM, Reed GT, Crocombe AD, Tjin SC. Structural health monitoring of bonded composite joints using embedded chirped fibre bragg gratings. Adv. Comp. Letters 2005;14/6:185-192.
22. Swart PL, Lacquet BM, Chtcherbakov AA. Chirped fiber Bragg grating sensor for pressure and position sensing. Opt. Eng. 2005;44/5: 054402(1-5)
23. Ussorio M, Wang H, Ogin SL, Thorne AM, Reed GT, Tjin SC, Suresh R. Modifications to FBG Spectra due to matrix cracking in a GFRP composite. Construct. Build. Mater. 2006;20/1 :111-118
24. OptiGrating, User's Reference and Tutorials, Integrated and Fiber Optical Gratings Design Software, (version 4.2), Optiwave Corporation, Canada

Figure captions:

Figure 1: (a) Schematic of a GFRP coupon with embedded CFBG sensor showing the two positions used to apply a through thickness compressive load to identify the low-wavelength end of the sensor. **(b)** Superposition of typical CFBG reflection spectra obtained when a GFRP coupon was loaded at positions 1 and 2.

Figure 2: Schematic diagram showing an edge view of the 60 mm overlap bonded joint with one adherend containing an embedded CFBG with a sensor length of 45 mm.

Figure 3: (a) View of the bonded section of a transparent GFRP lap joint after 8000 fatigue cycles; a disbond has initiated at A. **(b)** Comparison of CFBG reflected spectra at 2000 and 8000 cycles; disbond initiation has caused the low wavelength end of the reflected spectrum to shift to lower values.

Figure 4: The position of the CFBG-monitored disbond after (a) 9000 cycles, (b) 10,500 cycles and (c) 13,400 cycles.

Figure 5: Superposition of the reflected spectra after 9000, 10,500 and 13,400 cycles showing the movement of the dip in the spectrum to higher wavelengths (from B to D) as the disbond length increases.

Figure 6: Strain distribution in the region of the end of one adherend for a joint without a disbond. The white bands are the positions of the 90^0 plies.

Figure 7: Strain distribution along the fibre optic centre line position for the cases of no disbond, and disbond lengths of 5 mm and 10 mm.

Figure 8: Magnified view of the strain distribution towards the end of one adherend.

Figure 9: Strain distribution in the region of the end of one adherend for a joint with a disbond of 10 mm

Figure 10: Comparison of input strain for the optical modelling compared with the FE strain profile.

Figure 11: Predicted reflected spectrum for disbond lengths of (a) 5 mm and (b) 10 mm. The position of the disbond front is indicated by the short vertical line in each case.

Figure 12: Superposition of the predicted reflected spectra for disbond lengths of 5 mm and 10 mm.

Figure 13: Comparison of the disbond length obtained using the CFBG measurements with the disbond length measured from photographs of the bonded joint.

E (GPa)	ν
3	0.4

Table 1 – Adhesive material properties

E_1, GPa	E_2, GPa	E_3, GPa	G_{12}, GPa	G_{13}, GPa	G_{23}, GPa	ν_{12}	ν_{13}	ν_{23}
43	13	13	4	4	4.64	0.3	0.091	0.4

Table 2 – Composite ply material properties

Figures:

a)

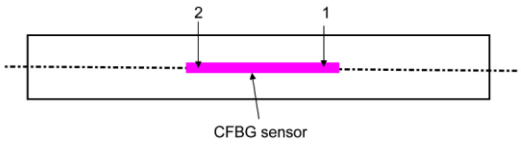

b)

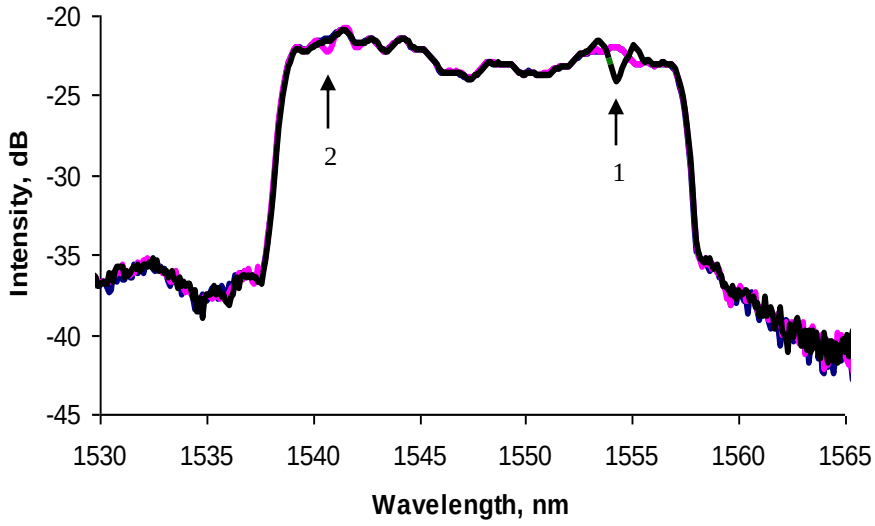

Figure 1

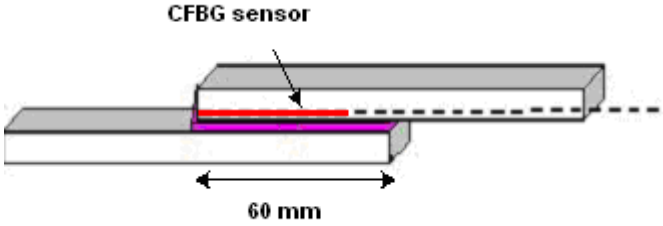

Figure 2

a) **b)**

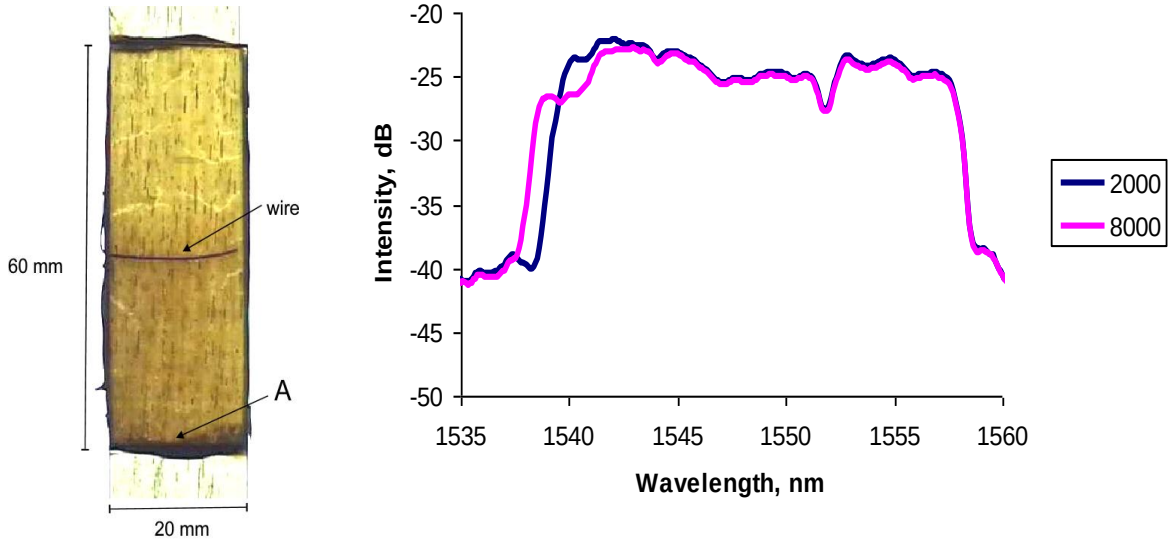

Figure 3

a) **b)** **c)**

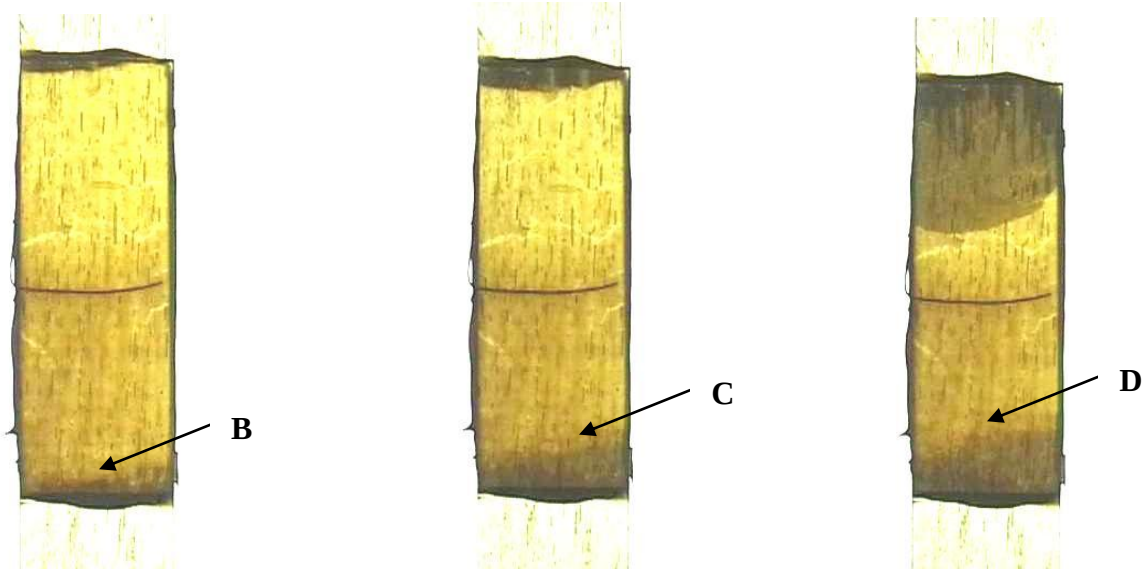

9000 cycles 10,500 cycles 13,400 cycles

Figure 4

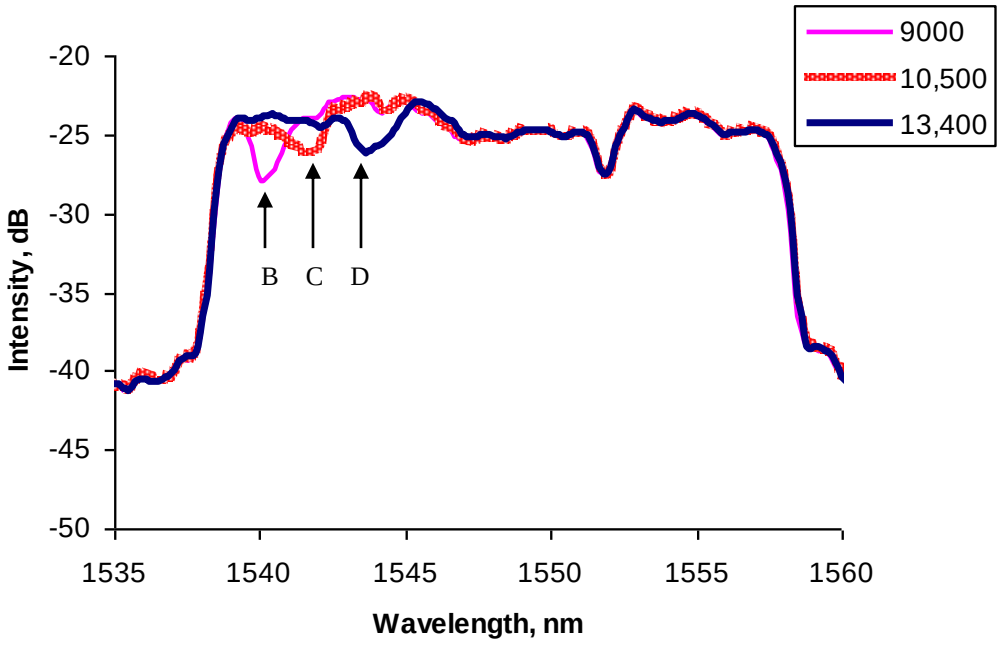

Figure 5

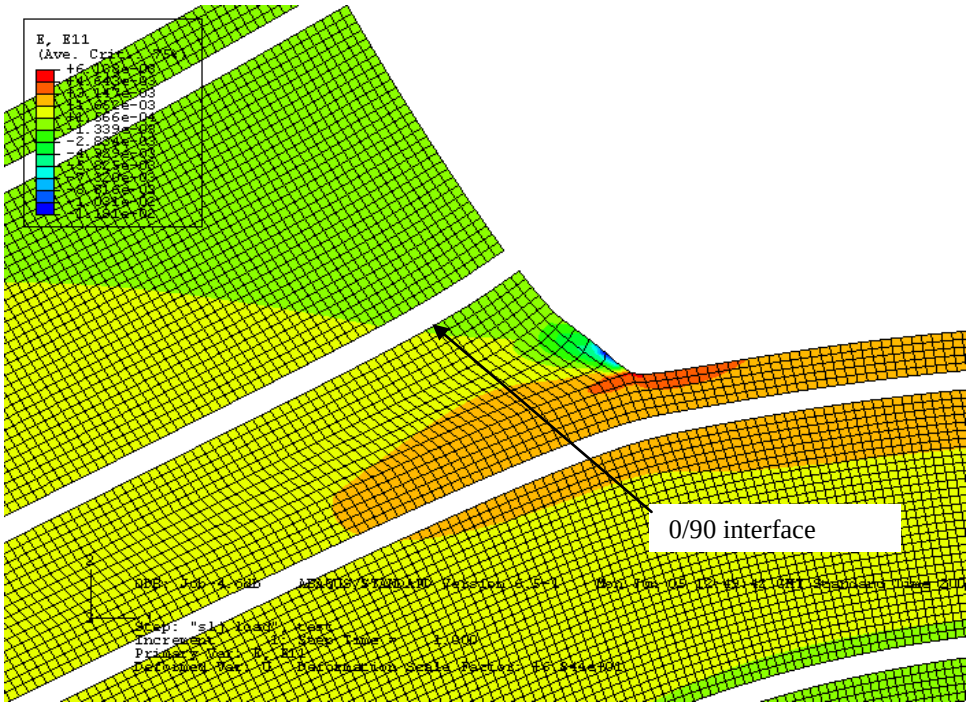

Figure 6

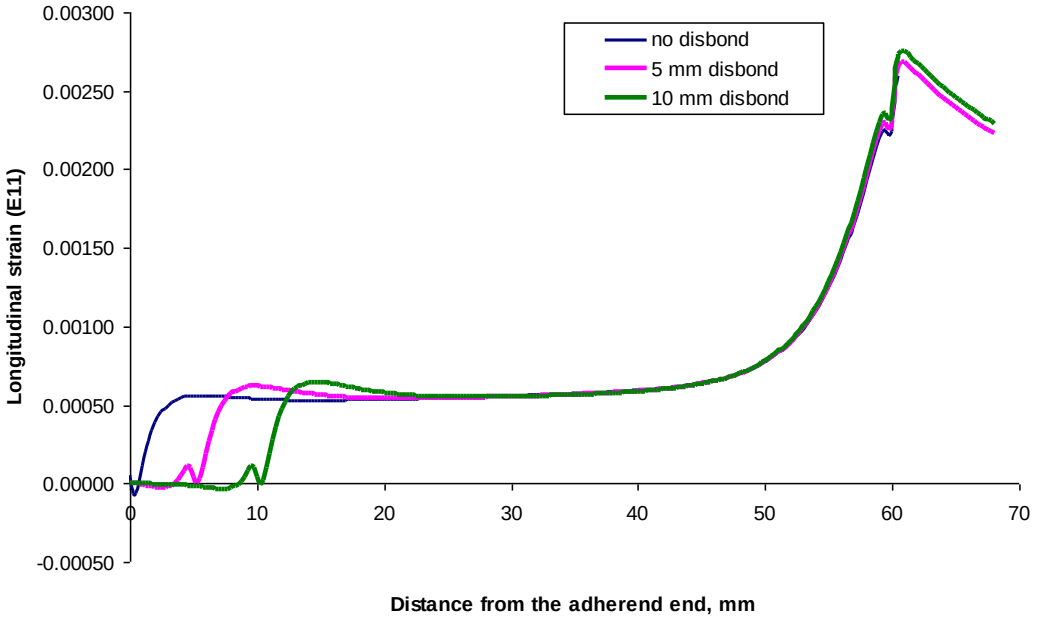

Figure 7

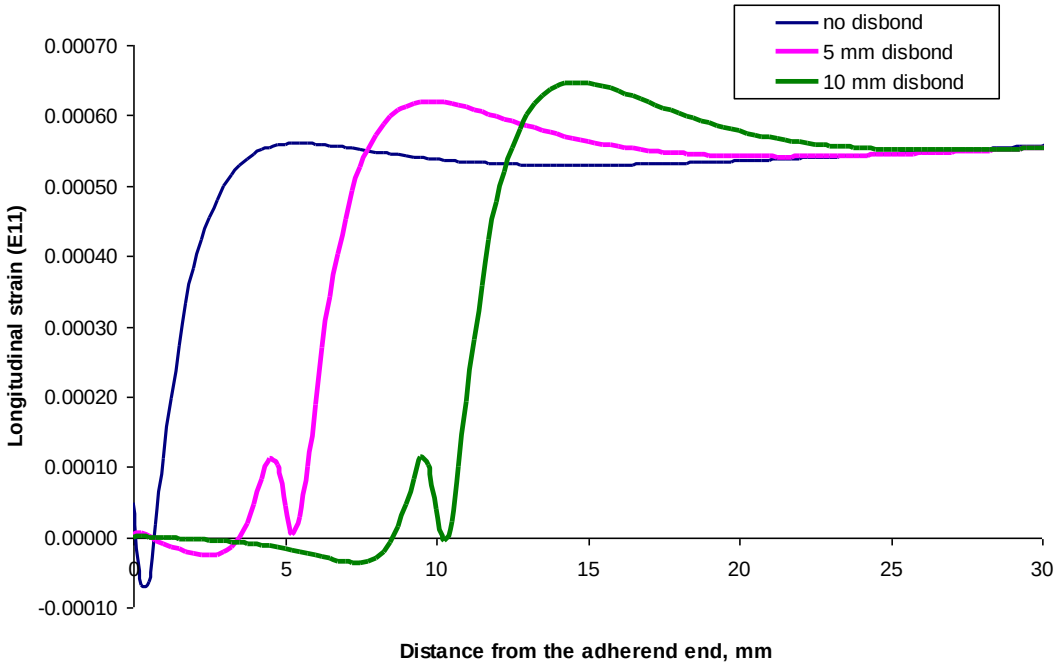

Figure 8

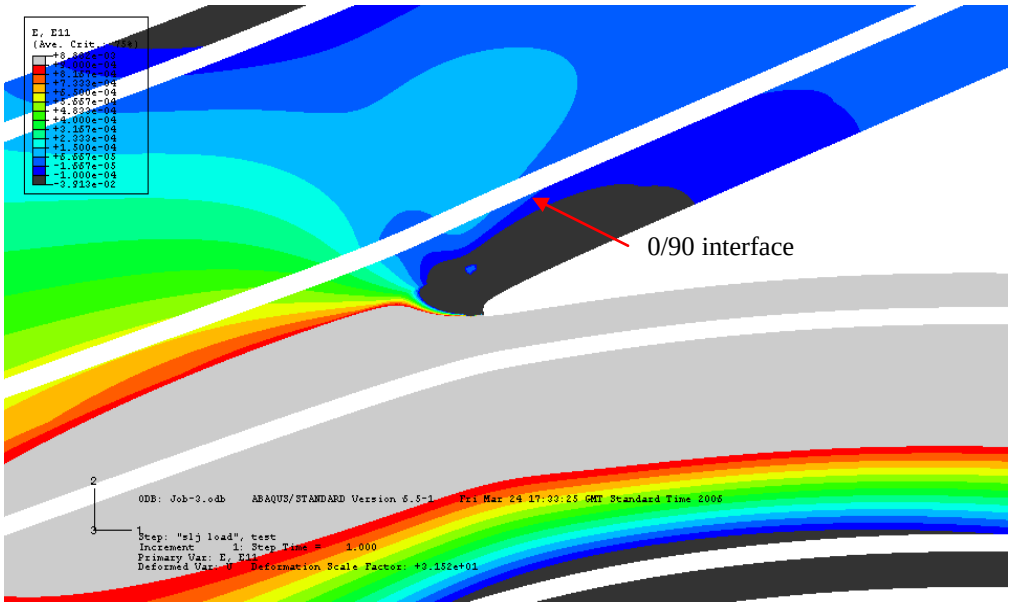

Figure 9

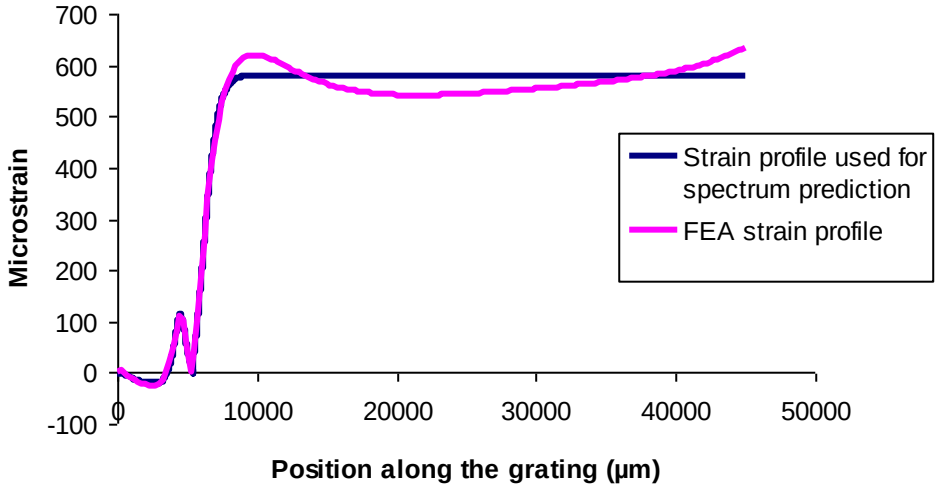

Figure 10

(a)

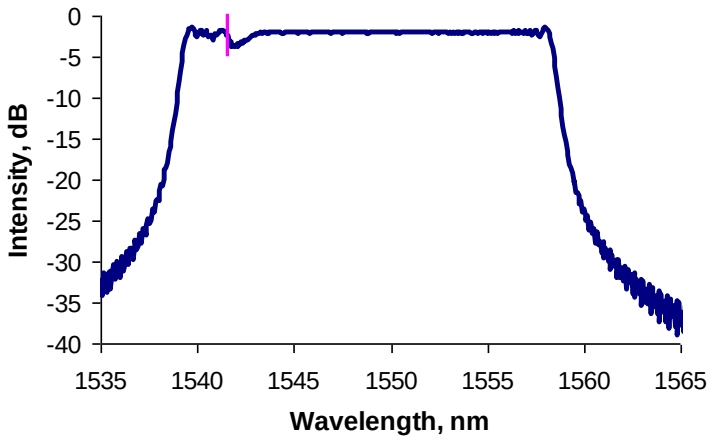
0
-5
-10
-15
-20
-25
-30
-35
-40
Intensity, dB
1535
1540
1545
1550
1555
1560
1565
Wavelength, nm

(b)

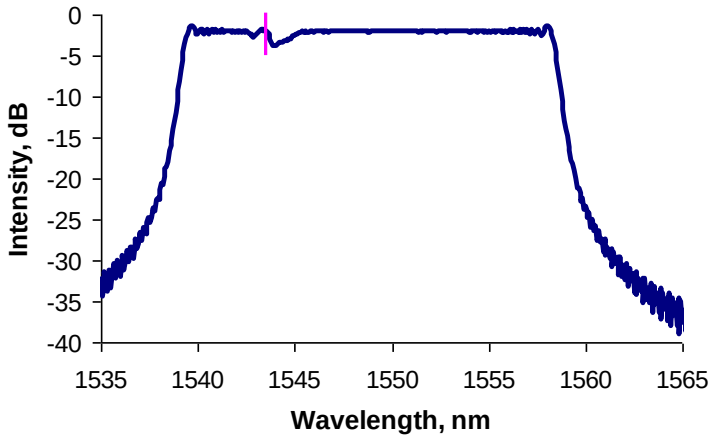
0
-5
-10
-15
-20
-25
-30
-35
-40
Intensity, dB
1535
1540
1545
1550
1555
1560
1565
Wavelength, nm

Figure 11

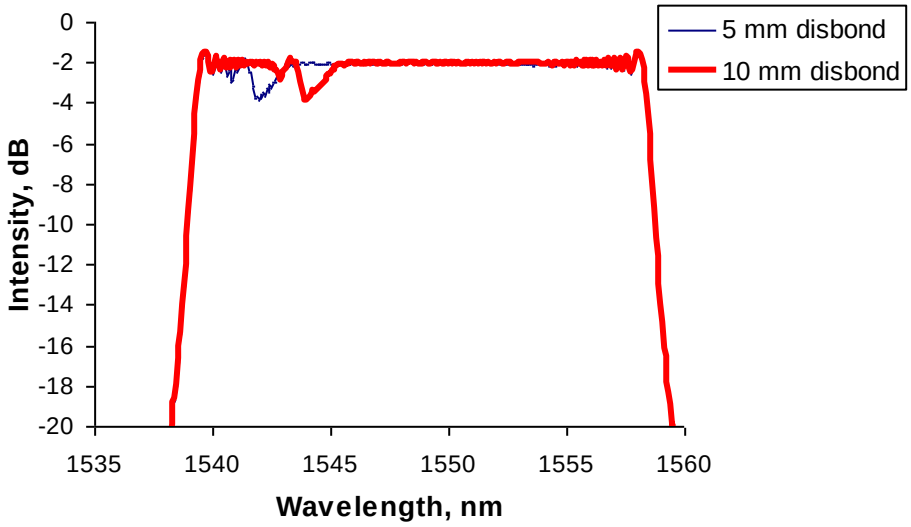

Figure 12

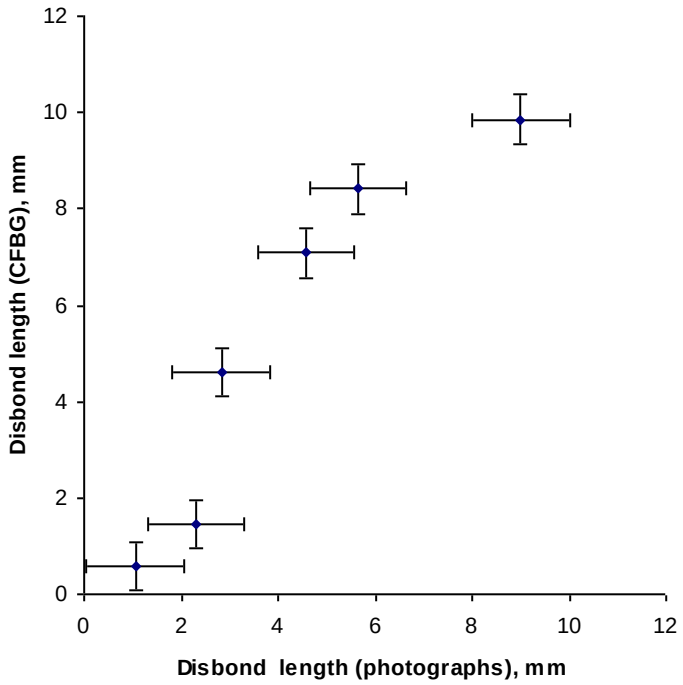

Figure 13